Engineering Applications of Artificial Intelligence 154 (2025) 110822

Contents lists available at ScienceDirect

Engineering Applications of Artificial Intelligence

journal homepage: www.elsevier.com/locate/engappai

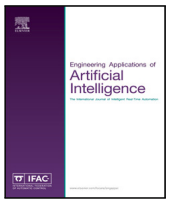

Research paper

Interpreting frequency evolution in ventricular fibrillation using embeddings and deep learning methods

Dafne Lozano-Paredes [a,*], Juan José Sánchez-Muñoz [b], Luis Bote-Curiel [a], Francisco M. Melgarejo-Meseguer [a], Antonio Gil-Izquierdo [c], F. Javier Gimeno-Blanes [c], José Luis Rojo-Álvarez [a]

[a] Universidad Rey Juan Carlos, Department of Signal Theory and Communications, Telematics, and Computing Systems, Cam. del Molino, 5, Fuenlabrada, 28942, Madrid, Spain
[b] Hospital Clínico Universitario Virgen de la Arrixaca, Arrhythmia and Electrophysiology Unit, Department of Cardiology, Ctra. Madrid-Cartagena, s/n, El Palmar, 30120, Murcia, Spain
[c] Universidad Miguel Hernández, Department of Signal Theory and Communications, Av. de la Universidad, s/n, Elche, 03202, Alicante, Spain

ARTICLE INFO

Keywords:
Ventricular fibrillation
Frequency evolution
Manifold learning
Deep learning
Electrocardiogram analysis
Interpretability

ABSTRACT

Recently, the necessity for advanced tools to scrutinize ventricular fibrillation (VF) has been highlighted. Despite progress in the field, applying deep learning techniques and manifold interpretations in clinical settings remains underexplored. This study aims to evaluate the effectiveness of low-dimensional embeddings for distinguishing VF. We analyzed VF from three clinical conditions: patients during cardiopulmonary bypass, dogs administered with different drugs, and implantable cardioverter defibrillator devices with varying offset characteristics. We employed several algorithms, including uniform manifold approximation and projection embeddings, temporal convolutional networks, fully connected networks, and Kolmogorov–Arnold networks. Our experiments revealed that VF dynamics can be categorized based on frequency evolution, and the result can be interpreted based on clinical knowledge. However, each dataset has unique characteristics, leading to variations in the best-performing method. These differences may arise because some VF types are more easily identifiable. Our findings prove that longer signals differentiate VF types more clearly as the frequency evolution becomes clearer over extended periods. Across the same dataset, methods showed only slight differences in performance. Notably, for one dataset, two different drugs in dogs showed similar frequency patterns. For the rest of the datasets and methods, accuracy ranged between 0.68 and 0.86, precision ranged from 0.69 to 0.84, recall ranged from 0.68 to 0.84, and F1 scores ranged from 0.68 to 0.84. We conclude that low-dimensional embeddings are an effective method for characterizing VF types, and these methods can support ongoing research that aims to clarify the mechanisms of VF.

1. Introduction

Cardiac arrhythmias are disruptions in the regular rhythm of the heart, often resulting in too-fast (tachycardia), too-slow (bradycardia), or erratic heartbeats. These disturbances can range from benign conditions to life-threatening emergencies. Arrhythmias can impair the heart's ability to pump blood effectively, leading to a cascade of health issues such as stroke, heart failure, and sudden cardiac arrest. Arrhythmias can originate in the atria or ventricles (Gaztañaga et al., 2012; Kingma et al., 2023). One of the most prevalent cardiac arrhythmias in individuals with sudden cardiac death (SCD) is ventricular fibrillation (VF), responsible for more than 80% of cases (Haïssaguerre, 2010). The failure of synchronized ventricular contraction due to rapid and chaotic electrical activity causes an instant decrease in cardiac output. To end VF, electrical defibrillation is currently the sole treatment available. Long-term VF causes the waveform amplitude to decrease, progressing from coarse to fine VF. As a result of the increasing consumption of myocardial energy stores, which leads to myocardial cell death, VF eventually degenerates into asystolia. Consequently, following a prolonged period of VF, the likelihood of effective defibrillation drops significantly (de Luna et al., 1989; John et al., 2012; Link et al., 2015).

Two primary hypotheses have been proposed to explain the mechanisms behind cardiac fibrillation: the multiple-wavelet hypothesis and the focal-source hypothesis. The multiple-wavelet hypothesis suggests that VF is characterized by multiple wandering wavelets within the

* Corresponding author.
E-mail address: dafne.lozanop@urjc.es (D. Lozano-Paredes).

https://doi.org/10.1016/j.engappai.2025.110822
Received 11 August 2024; Received in revised form 13 March 2025; Accepted 6 April 2025
Available online 5 May 2025

heart, observed through computerized mapping studies in large animals. This hypothesis proposes that steep action potential duration restitution and existing heart tissue heterogeneities work together to create wave breaks, sustaining VF (Moe et al., 1964; Garfinkel et al., 2000). In contrast, the focal-source hypothesis proposes that a stable mother rotor could generate rapid, localized activation. The fast activation rate from this rotor may cause conduction blocks, leading to sustained VF wavefronts (Jalife, 2000; Pandit and Jalife, 2013). To advance the understanding of VF dynamics, recent research has focused on developing advanced analytical methods, including the role of spectral analysis in enhancing our understanding of the electrophysiological features during VF episodes (Latcu et al., 2011). VF has been extensively studied for its various spectral and temporal characteristics, particularly concerning the multiple-wavelet and rotor theories of its mechanism (Nash et al., 2006). Recent research has further supported a paradigm of VF based on statistical fibrillatory dynamics, proposing equations that describe the behavior and number of wavelets and rotors observed during VF episodes (Dharmaprani et al., 2022).

Detection of VF using temporal (Arafat et al., 2011) and spectral characteristics has become a critical area of research, with methods such as fast Fourier transform (FFT) employed to analyze the frequency components of electrocardiogram (ECG) signals by estimating the power spectral density (PSD) (Afonso and Tompkins, 1995; Vaneghi et al., 2012). Algorithms employing band-pass digital filters with integer coefficients for VF and ventricular tachycardia (VT) detection have been developed for their simplicity and real-time efficiency (Jekova and Krasteva, 2004). Additionally, automatic diagnostic systems using temporal-frequency representation images of ECG signals have improved classification accuracy by removing the feature extraction stage in VF (Mjahad et al., 2018). Furthermore, other studies have focused on analyzing dominant frequencies and various parameters, including amplitude, bispectral analysis, amplitude spectrum area, wavelets, nonlinear dynamics, and N(α) histograms, in the context of VF detection to characterize the arrhythmia (Stewart et al., 1992; Amann et al., 2001). This type of frequency analysis has been instrumental in linking VF characteristics to resuscitation success, indicating that low-frequency ventricular fibrillation is associated with a low probability of effective resuscitation (Stewart et al., 1992). In a study comparing the spectral characteristics of electrical signals during sustained and non-sustained VF in patients with an implantable cardioverter-defibrillator (ICD), it was found that dominant frequency during the initial 3 s can differentiate between sustained and non-sustained VF (SánchezMuñoz et al., 2009). Moreover, additional spectral parameters can be estimated for each VF episode, including the peak power at the dominant frequency, an organization index, a bandwidth measurement, and an estimate of the correlation with a sinusoidal wave. It was found that these parameters were higher in induced VF episodes compared to spontaneous VF episodes (SánchezMuñoz et al., 2008). Despite these advancements, uncertainties remain regarding the exact progression and potential subtypes of VF based on different developmental stages.

Machine learning (ML) has revolutionized medicine and signal processing by offering powerful tools to analyze complex data, leading to significant advancements in diagnosis, treatment, and patient care. ML algorithms can identify complex patterns and dynamics within bioelectric signals, diagnose cardiac arrhythmias, including VF, and enhance patient outcomes and clinical interventions (Sahoo et al., 2020; Pham et al., 2021). For instance, one study extracted 14 VF metrics from ECG data, and a genetic algorithm was used as a feature selection technique to identify the optimal variables, followed by an ML classifier to distinguish between VF and VT, achieving high accuracy (Li et al., 2014). Similarly, QRS complex shape data have been combined with heart rate variability features to predict VF onset. By applying these measurements to neural networks, researchers found that the QRS complex shape significantly enhanced the accuracy of VF prediction (Taye et al., 2019). In addition to traditional ML approaches, deep learning has shown remarkable efficacy in arrhythmia detection. These efforts primarily focus on analyzing surface signals, including those from the 12-lead ECG and Holter monitoring systems. Some studies predict VF onset based on frequency metrics (Tseng and Tseng, 2020) or by incorporating time–frequency-based features into the model (Sabut et al., 2021). One notable application of deep learning involved using a convolutional neural network (CNN) to analyze spectral features of ECG to detect VF with 97% accuracy using the MIT-BIH dataset (Tseng and Tseng, 2020). Another significant study developed a deep learning model that combined long short-term memory (LSTM) and CNN layers, achieving 99.9% accuracy on the same database by utilizing temporal windows surrounding the beats as input features (Hassan et al., 2024). More recently, it has been proposed to integrate CNN, LSTM, and transformer models to classify arrhythmias based on ECG features, achieving 99.56% accuracy (Din et al., 2024). Their approach has three components. The first component extracts relevant features using deep learning, with a CNN capturing spatial features and a hybrid CNN-LSTM model capturing spatiotemporal features. A transformer model is then used to capture long-range temporal dependencies. The second component fuses these features and processes them in parallel with three base learners: random forest (RF), support vector machine (SVM), and logistic regression (LR). Finally, a majority voting classifier (ensemble learner) is applied to the concatenated features, further enhancing accuracy. Despite these advancements, manifold learning (MnL) techniques remain largely unexplored in ECG analysis, especially in VF research. Recently, a study demonstrated using MnL to distinguish between different VF types, showing that latent variables were more accurate VF descriptors than traditional temporal or frequency-domain features (Bernal Oñate et al., 2023). Unlike other ML techniques, such as tree-based methods or SVMs, which require feature extraction from bioelectric signals through heuristic methods, MnL provides a data-driven approach to extracting latent variables from biopotentials.

Our study builds on previous research that describes various potential mechanisms for VF. VF has been recognized as having a wide array of underlying substrates and phenotypes. Clinical insights are progressively identifying diverse mechanisms and ablation targets, emphasizing factors such as Purkinje or myocardial triggers, the temporal evolution of VF in hearts with no structural abnormalities, and the influence of localized substrate areas in cases involving structural heart disease. VF exhibits a range of scenarios and phenotypes in patients with structurally normal hearts, with distinct presentations often unique to each individual. While the fibrillating heart represents a dynamic and complex process, discrete sources frequently drive it, and catheter ablation has shown promise as a treatment option (Haïssaguerre et al., 2016; Walton et al., 2014). In this context, integrating advanced ML techniques with digital signal processing holds significant promise for advancing VF research and improving diagnostic and therapeutic capabilities. Our novel approach focuses on uncovering the heterogeneity within VF by identifying distinct subtypes based on frequency dynamics, whereas previous methods primarily aimed to distinguish VF as a singular condition and differentiate it from other arrhythmias. As previously mentioned, traditionally, bioelectric recordings have been analyzed using time-based features (e.g., cycle length, fragmentation), spectral features (e.g., fundamental and dominant frequencies, organization index), and entropy-based metrics (SánchezMuñoz et al., 2009, 2008). In contrast, our study emphasizes the frequency evolution of signals to differentiate these subtypes, avoiding reliance on ad hoc characteristics and making the methodology more generalizable. To achieve this, MnL techniques offer a powerful approach for introducing new feature dimensions, as they can distill the essence of signals into a reduced set of latent variables. Though these latent variables represent nonlinear combinations of the original input features, they can serve as valuable new features and be further examined to explore their physical and physiological implications. We hypothesize that MnL methods can enhance our understanding of VF by revealing distinct VF types characterized by unique frequency evolutions over time. Our

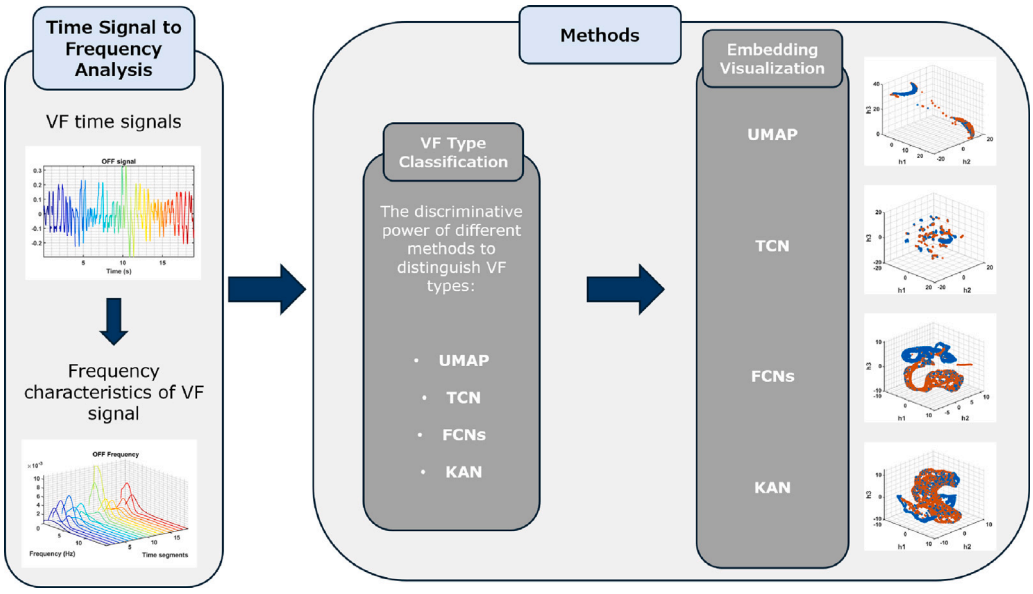

Fig. 1. General scheme of the methodology. The figure shows the steps followed in this work from left to right. The first block represents the time–frequency descriptive analysis in the Datasets Section. The second block shows the methods applied, where two steps are represented: first, the methods used for classification; and second, the methods used for visualization.

methodology consists of various approaches, including uniform manifold approximation and projection (UMAP) (McInnes et al., 2018), fully connected networks (FCNs) (Goodfellow et al., 2016), and deep learning methods such as temporal convolutional networks (TCN) (Bai et al., 2018) and Kolmogorov–Arnold networks (KAN) (Liu et al., 2024). This methodology effectively demonstrates the ability of manifold learning to reduce the dimensionality of complex VF data while preserving critical frequency-based features, making FV distinguishable. By integrating these approaches, the study not only seeks to classify VF subtypes but also provides interpretability into their dynamics. By clinically interpreting the embedding space, we aim to uncover new insights into the classification and pathophysiology of different VF types that conventional methods have not been able to detect so far. Our analysis focuses on signals of varying origins, lengths, and patterns, using three different datasets to ensure a comprehensive evaluation. This diverse data collection is a benchmark for detecting different VF types, allowing us to rigorously test and validate our methods. It also acknowledges that variations in dataset characteristics may influence the detection and differentiation of VF types and that certain VF types may not be distinguishable in some cases.

This document is organized as follows. Section 2 details the three datasets and the data acquisition and analysis methodologies. Then, Section 3 presents the results of the distinction of VF types, including classifiers, the embedding space representations, and a comparison with standard frequency metrics. Finally, Section 4 offers a discussion of the findings and the conclusions drawn from the study.

2. Materials and proposed method

As shown in Fig. 1, the first step of our process involved obtaining the frequency information from the raw VF time signals. Then, several methods were applied to check for distinctions between different VF types and to visualize the low-dimensional latent spaces generated by these methods.

2.1. Description of data sets

This study used three different datasets, each representing various types of patients or conditions. These are clinical datasets obtained from the Hospital Clínico Universitario Virgen de la Arrixaca; therefore, they are not publicly accessible at this time. The first data set includes human ECG recordings during cardiopulmonary bypass surgery (CPB), the second includes recordings during pharmacological administration of various substances in dogs, and the last includes ICD recordings from patients who experienced sustained and non-sustained VF. To analyze these datasets, we apply signal processing to obtain the frequency characteristics from the signals. Specifically, the FFT was applied to each signal or signal segment to compute the PSD. Therefore, we obtained frequency-based characteristics used as input to the models, focusing on the inherited structure of the signals.

This first dataset comprises ECG recordings obtained during CPB procedures. Specifically, it includes a dataset encompassing data from two distinct cardiac conditions occurring during VF in CPB, VFON, and VFOFF. In cardiac surgery, VFON episodes, prevalent during extracorporeal circulation, often depict a natural progression from VF to asystole. These occurrences were induced during post-aortic clamping and perfusion, with CPB conducted via cannulation in the ascending aorta and moderate hypothermia (28–32 °C) employed for myocardial protection using cold hyperkalemic blood cardioplegia administered via antegrade and retrograde routes. In contrast, VFOFF episodes originated from asystole following aortic declamping and restoration of cardiac circulation in patients. Each recording comprises one ECG lead sampled at 200 Hz. To ensure robust evaluation, the train–test split was implemented on the signals from 29 patients, resulting in distinct cases for each split, 17 cases for training (8 cases of VFON and 9 cases of VFOFF) and 12 cases for testing (4 cases of VFON and 8 cases of VFOFF). The analysis encompassed frequency-based approaches in which signals were segmented using overlapping windows, and the Welch periodogram method was applied. The 10 windows were selected to capture the frequency evolution over time, resulting in an effective window length of 2 s.

The second dataset involved a study of 23 anesthetized mongrel dogs administered various pharmacological agents: amiodarone, diltiazem, flecainide, and a control group. VF was induced by electrical pacing through a catheter electrode in the right ventricle. ECG signals were recorded continuously for 6 min. Group 1 (5 dogs) served as the control group with no prior drug administration, group 2 (5 dogs) received amiodarone at a dose of 5 mg/kg, group 3 (7 dogs) received diltiazem at 0.2 mg/kg, and group 4 (5 dogs) received flecainide at 2 mg/kg. Drugs were chosen based on their effects on molecular and

electrophysiological changes during VF. Specifically, amiodarone treats life-threatening arrhythmias unresponsive to other drugs by relaxing heart muscles and decreasing certain ionic currents. Diltiazem, a calcium channel blocker, manages high blood pressure and angina by relaxing blood vessels and improving heart oxygenation. Flecainide is an antiarrhythmic drug that prevents severe ventricular arrhythmias and stabilizes cardiac rhythm by slowing electrical signals in the heart. Each recording comprises one ECG lead sampled at 1000 Hz. To ensure robust evaluation, the train–test split was implemented on the signals from 23 dogs, resulting in distinct cases for each split, 14 cases for training (3 cases of amiodarone, 4 cases of flecainide, 4 cases of diltiazem, and 3 control cases) and 9 cases for testing (2 cases of amiodarone, 2 cases of flecainide, 3 cases of diltiazem and 2 control cases). The analysis encompassed frequency-based approaches in which signals were segmented using overlapping windows, and the Welch periodogram method was applied. Ten windows were selected to capture the frequency evolution over time, resulting in an effective window length of 1 s.

The third dataset includes patients who experienced at least one sustained VF episode requiring defibrillation and at least one non-sustained VF episode, both of which were induced and recorded by the ICD. Sustained VF episodes require an electrical shock to terminate the arrhythmia, while non-sustained VF episodes resolve naturally without intervention. The dataset consists exclusively of induced VF episodes, each recording sampled at 128 Hz from the ICD. For robust evaluation, a train–test split was performed on 74 episodes, resulting in distinct cases for each split, 60 cases for training (40 sustained VF and 20 non-sustained VF) and 14 cases for testing (9 sustained VF and 5 non-sustained VF). Given that the signals have a mean duration of 7.3731 s, we examined the frequency spectrum of complete signal datasets without using segmented windows with overlapping intervals. This approach ensures the reliability of our analysis by capturing the complete spectral characteristics of uninterrupted signal sequences.

Fig. 2 presents an initial exploratory analysis of the datasets incorporated in this study. These datasets constitute the input space for the models and methodologies applied. Although not exhaustive, the exploratory analysis shown in this figure shows an example of the temporal and frequency space representation for each of the three datasets evaluated. In particular, under the denominations (a) and (b), the representation in time and frequency of two paired signals (VFON and VFOFF) corresponding to the first surgical dataset is presented. The corresponding ones are presented under the denominations (c) and (d) with the paired analysis of an example of the dataset of dogs treated with diltiazem versus those treated with flecainide. Finally, the illustrative example of the third set of data that involves the signals corresponding to the classification of Sustained and Non-sustained VF is depicted on panels (e) and (f). In the first column of the figure, four graphs are presented under a single denomination, panels (a), (c), and (e), for each of the three datasets. In these three blocks of four graphs, the left column includes the temporal representation of the two paired signals for the two classes in rows. In the right-hand column, still within the left block, a spectral representation of the different segments into which the temporal signal was divided is shown. For the reader's convenience, the temporal illustration of the signal is represented with different segment colors. These colors correspond to their respective spectral analyses in their proper wire-framed representation. In case (e), corresponding to the example of the Sustained and Non-sustained VF dataset, the temporal limitation of the signal has suggested its representation in a single segment. Finally, to offer a more illustrative comparative view, the superposition of the wire-frame spectral figures of both classes of signals has been incorporated in the right-hand column, on panels (b), (d), and (f), where in this case, the colors have been made to correspond with the classes analyzed.

Visual inspection of Fig. 2 allows us to observe that in the case of surgical signals, the spectrum of VFOFF seems to contain a higher spectral content than VFON. Although less intense, this situation seems repeated for the Flecainide vs. Diltiazem classes in the second data set from dogs. Finally, in the case of the third set of data, and for the example incorporated in this exploratory analysis, a clear bimodality is seen in the case of non-sustained VF, with a greater participation of the low-frequency lobe. In contrast, in the case of sustained VF, a single prevalent modality is observed in the high-frequency band where the second lobe of Non-Sustained appeared. At this point, it is necessary to state that the examples shown here have been selected among all existing datasets for illustrative purposes. So, they cannot be considered generalizable over the dataset. Still, they do suggest that there may be underlying intrinsic differences that could be evaluated under the appropriate machine learning evaluation.

With each dataset, we can represent the data in the form of a matrix $\mathbf{X} \in \mathbb{R}^{M \times N}$. In this case, the nth column of the matrix, $\mathbf{x}_{\cdot n}$, is a $M \times 1$ column vector containing the frequency observations of each of the M patients samples. The mth row, $\mathbf{x}_{m\cdot}$, is a $1 \times N$ row vector with the frequency observations for the mth patient. The element $x_{m,n}$ is the frequency observation for the mth patient and the nth frequency information. For the dataset involving a binary classification problem, $\mathbf{y} \in \{0,1\}^{M \times 1}$ represents the column vector that identifies the class or label: 1 for VFON in the CBP dataset or sustained VF in the ICD dataset, and 0 for VFOFF in the CBP dataset or non-sustained VF in the ICD dataset. In the case of a multiclass classification problem, $\mathbf{y} \in \{0,1,2,3\}^{M \times 1}$ represents the different drugs administered to the dogs, with each value corresponding to a specific drug treatment category.

2.2. Estimating embeddings

Data representation in a latent space is crucial for extracting meaningful patterns and features from complex datasets. Hence, our methodology focuses on comparing different methods to evaluate the identification of various types of VF, measuring performance using metrics, and visually representing the dimensional reduction structure for each method. UMAP was chosen for its topological capabilities, allowing us to capture complex, high-dimensional relationships in a lower-dimensional space. TCN was employed for its convolutional nature, which is well-suited for modeling sequential data and frequency pattern evolution in the signals. FCNs were included due to their versatility and ability to model complex interactions across features. KANs were selected for their interpretability, offering insights into the underlying dynamics through activation functions.

UMAP is an advanced dimensionality reduction technique known for its efficiency and scalability (McInnes et al., 2018). When analyzing this kind of data in the high-dimensional space, other dimensionality reduction methods, such as PCA, may struggle because it primarily captures linear relationships, and t-SNE can capture nonlinear relationships but can be computationally inefficient due to the high dimensional data. Then, UMAP is an appropriate method to analyze data on such characteristics in which extensive datasets and nonlinear characteristics appear. One of its key features is its ability to preserve both local and global structures within the data, ensuring that relationships between data points remain consistent even after dimensionality reduction. UMAP achieves this by creating a graph that connects nearby data points based on their distance or similarity in the high-dimensional space. It then optimally places these points in a lower-dimensional space, minimizing the differences in distances between the original and reduced representations. This process maintains the local and intrinsic structures of the data.

For the mathematical formulation of UMAP, we consider our previously defined dataset as $\mathbf{X} \in \mathbb{R}^{M \times N}$. Let $\mathbf{x}_{m_1\cdot}$ and $\mathbf{x}_{m_2\cdot}$ denote two data points in this dataset, located in the high-dimensional space $\mathbb{R}^N$. After the reduction to 3 dimensions, in the embedding space, we have $\mathbf{Z} \in \mathbb{R}^{M \times 3}$. To determine which data points are considered neighbors in

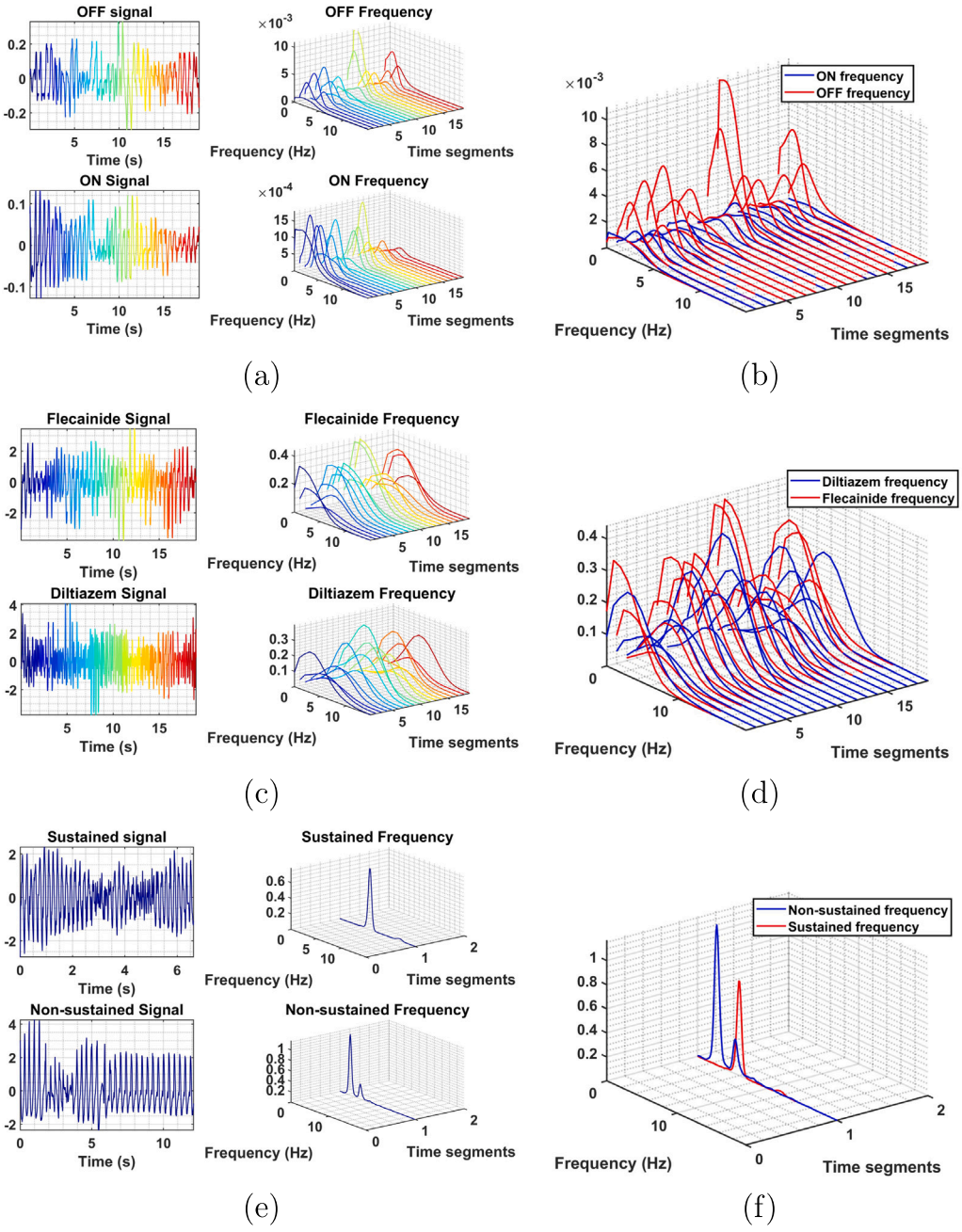

Fig. 2. The left column shows the correspondence between time segments and their frequency representations. The right column compares input spaces, illustrating two signals per dataset. In the first row, (a) and (b) illustrate the time–frequency analysis (VFON and VFOFF) corresponding to the surgical dataset. In the second row, (c) and (d) correspond with the paired analysis of an example of the dataset of dogs treated with diltiazem versus those treated with flecainide. In the last row, (e) and (f) correspond to the classification of Sustained and Non-sustained VF.

the high-dimensional space, the conditional probability $p_{m_2|m_1}$ that $\mathbf{x}_{m_2.}$ is selected as a neighbor of $\mathbf{x}_{m_1.}$ is defined as:

$$p_{m_2|m_1} = exp\left[\frac{-d(\mathbf{x}_{m_1.}, \mathbf{x}_{m_2.}) - \rho_{m_1}}{\sigma_{m_1}}\right], \tag{1}$$

where σ_{m_1} is the perplexity parameter influencing the effective number of neighbors considered from a given point. On the other hand, ρ_{m_1} can be interpreted as the average weighted distance between a specific point and its neighboring points. We use $d(\mathbf{x}_{m_1.}, \mathbf{x}_{m_2.})$ to denote the distance metric measuring the separation between $\mathbf{x}_{m_1.}$ and $\mathbf{x}_{m_2.}$ in the dataset. An essential distinction in the probability distributions of UMAP lies in its unique local distance metric customized for each pair of points. The distance probability in UMAP low-dimensional space is defined as:

$$q_{m_1,m_2} = (1 + a\|\mathbf{h}_{m_1} - \mathbf{h}_{m_2}\|^{2b})^{-1}, \tag{2}$$

where $\mathbf{h}_{m_1}$ and $\mathbf{h}_{m_2}$ represent the embeddings of data points $\mathbf{x}_{m_1.}$ and $\mathbf{x}_{m_2.}$ in the low-dimensional space and a and b are parameters controlling the shape and scaling of the distribution.

TCNs are networks structured with one or more blocks of one-dimensional convolutional (1D-CONV) layers. These layers use dilated convolutions, where the filter is applied to input data points spaced apart by a certain number of steps, determined by a dilation factor. This dilation factor increases the receptive field, allowing the network to capture dependencies between distant frequency steps. When calculating the output at a frequency step s in causal TCNs, a CONV layer only

considers previous frequency steps (1 to $s-1$). In a dilated causal 1D-CONV layer, the convolution operation F at location s of the sequence and a filter $f : \{0,\dots,k-1\} \to \mathbb{R}$ is provided by the following equation:

$$F(s) = \left(\mathbf{x}_{m\cdot} *_d f\right)(s) = \sum_{i=0}^{k-1} f(i) \cdot x_{m,s-d\cdot i}, \tag{3}$$

where $\mathbf{x}_{m\cdot}$ is the layers input, $*_d$ is the convolution operation, d is the dilation factor, k is the filter size, and $s - d \cdot i$ accounts for the past directions. In TCNs with L layers, each layer successively applies dilated convolutions, extracting hierarchical features from the input $\mathbf{x}_{m\cdot}$. This hierarchical feature extraction process leads to a progressive reduction of dimensionality $\mathbf{h}_m$ of $\mathbf{x}_{m\cdot}$.

FCNs are employed to reduce the dimensionality of the input data. The FCN operates by transforming the high-dimensional input data through several layers, with each layer progressively reducing the number of features until the bottleneck is reached. The bottleneck layer is a compact input data representation, capturing the most critical features for the classification task. Moreover, visualizing the structure given by the bottleneck can provide insights into the reduction process. A direct representation is provided for a bottleneck of size 3, while for higher bottlenecks, the reduction to 3 dimensions is performed using UMAP. After this dimensionality reduction phase, a subsequent part of the network acts as a classifier to perform the final classification task based on the compressed information. Mathematically, the input data $\mathbf{x}_{m\cdot}$ is compressed by the first layers of the FCN into an encoding symbol $\mathbf{h}_m$, given by

$$\mathbf{h}_m^{(L)} = \phi^{(L)}(\mathbf{W}_e^{(L)}\mathbf{h}_m^{(L-1)} + \mathbf{b}_e^{(L)}), \tag{4}$$

where $\phi^{(L)}$ is a nonlinear transformation, $\mathbf{W}_e^{(L)}$ is the weight matrix and $\mathbf{b}_e^{(L)}$ is the bias vector of the encoder at layer L. The reduction of dimensionality at Lth layer in the latent space corresponding to the input $\mathbf{x}_{m\cdot}$ is indicated by $\mathbf{h}_m^{(L)}$.

An additional approached method consists of KANs, which can be considered an alternative to Multi-Layer Perceptrons (MLPs) by introducing a fundamentally different approach to activation functions. Unlike MLPs, which use fixed activation functions at each node (*neuron*), KANs utilize learnable activation functions applied to the edges (*weights*). This design eliminates using linear weights; instead, every weight parameter is replaced by a univariate function, typically parameterized as a spline. The theoretical foundation of KANs comes from the Kolmogorov–Arnold representation theorem, which states that any multivariate continuous function ($f : [0,1]^n \to \mathbb{R}$) can be represented as a superposition of continuous functions of a single variable. Mathematically, this can be expressed as:

$$f(\mathbf{x}_{m\cdot}) = \sum_{q=1}^{2n+1} \boldsymbol{\Phi}_q \left(\sum_{p=1}^{n} \varphi_{q,p}(x_{m,p}) \right), \tag{5}$$

where $\phi_{q,p} : [0,1] \to \mathbb{R}$ and $\boldsymbol{\Phi}_q : \mathbb{R} \to \mathbb{R}$. In this formulation, $\boldsymbol{\Phi}_q$ and $\varphi_{q,p}$ are learnable activation functions, making the network adaptable to various data distributions and feature interactions. The composition of these functions can summarize the overall function of a KAN, then a L-layer KAN can be defined as:

$$\mathrm{KAN}(\mathbf{x}_{m\cdot}) = \left(\boldsymbol{\Phi}_{L-1}\circ\boldsymbol{\Phi}_{L-2}\circ\cdots\circ\boldsymbol{\Phi}_1\circ\boldsymbol{\Phi}_0\right)\mathbf{x}_{m\cdot}, \tag{6}$$

where $\boldsymbol{\Phi}_i$ represents the ith layer of the complete KAN network. For each layer with n_{in} -dimensional input and n_{out} -dimensional output, $\boldsymbol{\Phi}$ consist of $n_{\text{in}} \times n_{\text{out}}$ 1-D learnable activation functions $\phi_{q,p}$,

$$\boldsymbol{\Phi} = \left\{\phi_{q,p}\right\}, \quad p = 1,2,\dots,n_{\text{in}}, \quad q = 1,2\cdots,n_{\text{out}}. \tag{7}$$

This approach allows KANs to effectively capture and model complex, nonlinear relationships within the data, improving accuracy and interpretability since the learned activation functions can offer insights into the specific transformations and relationships the network has identified. As in MLPs, we can obtain activations from KANs during training and generate embeddings of these learnable features. These embeddings enable us to conduct similarity assessments with the other methodologies, thereby evaluating the effectiveness of the learning process.

2.3. Frequency characteristics of the signals

Analyzing frequency metrics such as the dominant frequency, fundamental frequency, and the second and third harmonics of the signal (Barquero-Pérez et al., 2010; SánchezMuñoz et al., 2009) is an established method for assessing differences between various signal types. This analysis can help compare our proposed methodology with classifications based on these metrics. The metrics are calculated using the signal PSD, representing signal power distribution across different frequency components $\mathbf{f}_{m\cdot}$. The dominant frequency is the frequency at which the signal power peaks, indicating the most significant feature and where the majority of the signal energy is concentrated: $f_d = \arg\max \mathbf{f}_{m\cdot}$. Moreover, the fundamental frequency, the lowest frequency of a periodic waveform, defines the primary rhythmic pattern of the signal. Alongside the fundamental frequency, the bandwidth around it indicates the range of frequencies that hold significant energy close to the fundamental frequency. Additionally, the second and third harmonics, integer multiples of the fundamental frequency, provide deeper insights into the signal structure and complexity. The second harmonic is twice the fundamental frequency, while the third harmonic is three times the fundamental frequency. These harmonics help identify the periodic components of the signal and reveal any distortions or additional patterns.

3. Experiments and results

3.1. Results on class separation

In this research, we explored diverse techniques to detect VF in various datasets. These methods included UMAP for latent space representation, TCNs, FCNs with varying bottleneck sizes (3, 5, 10, and 15) and KAN to optimize feature extraction and classification. We assessed the performance of these classifiers using standard metrics like accuracy, precision, recall, and F1-score. Our goal is to characterize VF subtypes by identifying frequency evolutions over time and determining an operational detection threshold. Since we classify individual frequency segments within a signal, some misclassifications may occur. However, the overall frequency progression remains identifiable, making a 70% accuracy threshold sufficient for meaningful subtype differentiation while accounting for intrinsic signal variability. Additionally, lower performance metrics can indicate minimal or no differences between VF subtypes under certain conditions, so they are also considered. Additionally, we compared our approach to traditional methods based on dominant and fundamental frequencies to gauge its effectiveness. We will also consider LSTM networks to compare the performance of our proposed networks with that of well-established methods.

Table 1 summarizes the performance metrics for each classifier with the surgical VF data. UMAP demonstrated good performance with an overall accuracy of 0.79, balanced precision, and recall across both classes. TCNs achieved an accuracy of 0.68. They offered stable performance with a balanced precision and recall for class C1 (VFOFF), but struggled with class C2 (VFON), as indicated by a lower recall (0.60). Finally, for FCNs with a bottleneck size of 3, the network achieved an accuracy of 0.78 and slightly higher performance in recall for class C1. With bottleneck 5, an accuracy of 0.79 was achieved. For the bottleneck of 10, the highest accuracy was obtained with a value of 0.81, so this larger bottleneck retained more information, capturing essential features. Similar to FC n10, the FC n15 achieved an accuracy of 0.80 and showed high recall for class C1. Finally, KAN obtained lower metrics compared to the best-performing methods but remained within the range of the TCN. In Table 2 appear the results for the

Table 1
Performance metrics for the surgical VF data for UMAP, TCN, and FCNs with different bottleneck sizes (3, 5, 10, and 15), and KAN. Class C1 (VFOFF) and class C2 (VFON).

	UMAP	TCN	FC n3	FC n5	FC n10	FC n15	KAN
Accuracy	0.79	0.68	0.78	0.79	0.81	0.80	0.67
Precision C1	0.85	0.64	0.76	0.77	0.77	0.75	0.63
Precision C2	0.75	0.73	0.79	0.81	0.87	0.85	0.74
Macro precision	0.80	0.69	0.78	0.79	0.82	0.80	0.67
Recall C1	0.73	0.77	0.80	0.82	0.87	0.85	0.70
Recall C2	0.86	0.60	0.76	0.77	0.77	0.76	0.64
Macro recall	0.80	0.68	0.78	0.80	0.82	0.81	0.67
F1 score C1	0.79	0.70	0.78	0.79	0.81	0.80	0.66
F1 score C2	0.80	0.68	0.77	0.79	0.82	0.81	0.68
Macro F1 score	0.79	0.68	0.78	0.79	0.81	0.80	0.67

Table 2
Performance metrics using frequency metrics method for surgical VF data.

	Class C1	Class C2	Macro average
Precision	0.76	0.69	0.72
Recall	0.67	0.77	0.72
F1 Score	0.71	0.73	0.72
Accuracy		0.72	

Table 3
Performance metrics for UMAP, TCN, and FCNs with different bottleneck sizes (3, 5, 10, and 15), and KAN for the data comparing VF signals in dogs treated with different drugs. Class C1 (Flecainide), Class C2 (Amiodarone), Class C3 (Diltiazen), Class C4 (Controls).

	UMAP	TCN	FC n3	FC n5	FC n10	FC n15	KAN
Accuracy	0.57	0.63	0.56	0.59	0.59	0.59	0.57
Precision C1	0.48	0.43	0.62	0.57	0.50	0.66	0.55
Precision C2	0.52	0.31	0.28	0.43	0.51	0.34	0.38
Precision C3	0.65	0.89	0.71	0.74	0.72	0.70	0.68
Precision C4	0.60	0.72	0.55	0.55	0.59	0.59	0.55
Macro precision	0.56	0.59	0.54	0.57	0.58	0.57	0.55
Recall C1	0.62	0.59	0.44	0.44	0.44	0.45	0.53
Recall C2	0.38	0.19	0.46	0.49	0.50	0.51	0.36
Recall C3	0.76	0.81	0.71	0.74	0.75	0.75	0.71
Recall C4	0.44	0.85	0.56	0.64	0.65	0.61	0.57
Macro recall	0.55	0.61	0.54	0.58	0.58	0.58	0.54
F1 score C1	0.54	0.50	0.52	0.50	0.47	0.53	0.52
F1 score C2	0.44	0.24	0.35	0.46	0.50	0.41	0.36
F1 score C3	0.70	0.85	0.71	0.74	0.73	0.72	0.69
F1 score C4	0.51	0.78	0.55	0.59	0.62	0.60	0.56
Macro F1 score	0.55	0.59	0.53	0.57	0.58	0.57	0.54

Table 4
Confusion matrix illustrating the difficulty in distinguishing between C1 (flecainide) and C2 (amiodarone) in the TCN model.

		Predicted classes			
		Flecainide	Amiodarone	Diltiazen	Controls
Actual classes	Flecainide	295	159	20	4
	Amiodarone	205	184	71	18
	Diltiazen	57	3	542	115
	Controls	60	8	202	208

classical frequency methods employed in the same dataset. The FC n10 model achieved the highest accuracy at 0.81, compared to 0.72 for this classical method. This indicated a significant improvement in correctly identifying VFON and VFOFF instances.

The classification task involved four classes based on different treatments for the dataset of VF signals in dogs treated with various drugs. As shown in Table 3, UMAP demonstrated moderate performance with an overall accuracy of 0.57. It showed balanced precision and recall across the four classes. However, it struggled significantly with identifying class C1 (flecainide) and class C2 (amiodarone), as indicated by lower precision and recall values. TCN achieved better overall

Table 5
Performance metrics using frequency metrics method for VF detection based on different drugs.

	Class C1	Class C2	Class 3	Class C4	Macro average
Precision	0.48	0.42	0.67	0.65	0.56
Recall	0.59	0.36	0.74	0.51	0.55
F1 score	0.53	0.39	0.70	0.57	0.55
Accuracy			0.57		

Table 6
Performance metrics for UMAP, TCN, and Fully Connected Networks with different bottleneck sizes (3, 5, 10, and 15), and KAN for the data comparing VF signals in DAI. Class C1 (sustained VF) and Class C2 (non-sustained VF).

	UMAP	TCN	FC n3	FC n5	FC n10	FC n15	KAN
Accuracy	0.86	0.79	0.71	0.71	0.71	0.71	0.66
Precision C1	0.89	0.88	0.67	0.67	0.67	0.67	0.60
Precision C2	0.80	0.67	0.80	0.80	0.80	0.80	0.72
Macro precision	0.84	0.77	0.73	0.73	0.73	0.73	0.66
Recall C1	0.89	0.78	0.86	0.86	0.86	0.86	0.74
Recall C2	0.80	0.80	0.57	0.57	0.57	0.57	0.56
Macro recall	0.84	0.79	0.71	0.71	0.71	0.71	0.65
F1 score C1	0.89	0.82	0.75	0.75	0.75	0.75	0.65
F1 score C2	0.80	0.73	0.67	0.67	0.67	0.67	0.63
Macro F1 score	0.84	0.78	0.71	0.71	0.71	0.71	0.64

performance with an accuracy of 0.63, and class C3 showed the highest precision and recall. However, again, the model faced challenges with class C2 and class C1, where the precision and recall for class C2 were particularly low (precision of 0.31 and recall of 0.19). The results for FCNs with different bottleneck dimensions varied. FC n3 achieved an accuracy of 0.56, FC n5 showed a slight improvement with an accuracy of 0.59, and FC n10 and FC n15 maintained the same accuracy of 0.59 with slightly improved macro-averaged metrics. Finally, KAN, with an accuracy of 0.57, achieved a performance similar to UMAP and FC networks. Despite these varied performances, all FCNs demonstrated difficulty in accurately distinguishing between class C1 and class C2.

It is valuable to visualize the confusion matrix to gain further insights into the classification challenges, particularly the confusion between class C1 (flecainide) and class C2 (amiodarone). Given the relatively better performance of the TCN, we have selected TCN for this visualization, as shown in Table 4. Here, we can observe the confusion between class C1 and class C2, probably indicating a similar frequency evolution.

In comparison with the classification based on classical frequency metrics, the accuracy of the proposed models was similar to this method, with most models achieving around 0.57 to 0.63, while the classical method accuracy was 0.57 as shown in Table 5. TCNs offered notable improvements in precision, recall, and F1 scores for certain classes, but they underperformed in others. The overall macro averages for precision, recall, and F1 scores were comparable between the proposed models and the classical methods. This indicates that the proposed approach can be as effective as classical frequency-based methods, with specific advantages in certain areas.

For the final dataset, the performance metrics for UMAP, TCN, FCNs and KAN with different bottleneck sizes indicate varying degrees of effectiveness in recognizing two types of VF, sustained and non-sustained (see Table 6). UMAP demonstrated good overall accuracy (0.86) and balanced performance for both classes, showing its effectiveness at classifying both classes with high macro precision and recall. TCN achieved an accuracy of 0.79. The FCNs, regardless of bottleneck size (3, 5, 10, and 15), showed a consistent overall accuracy of 0.71 and similar metrics across all configurations. This consistency indicates that increasing the bottleneck size did not improve the model performance, and the FCNs displayed balanced precision and recall for both classes. However, KAN obtained the lowest performance among all methods,

Table 7
Performance metrics using frequency metrics method for sustained and non-sustained VF.

	Class C1	Class C2	Macro average
Precision	0.84	0.70	0.77
Recall	0.84	0.70	0.77
F1 score	0.84	0.70	0.77
Accuracy		0.79	

Table 8
Performance metrics of the LSTMs for all the datasets.

	Surgical FV	Dogs FV	DAI FV
Accuracy	0.79	0.59	0.71
Precision C1	0.76	0.48	0.60
Precision C2	0.83	0.49	0.78
Precision C3	–	0.68	–
Precision C4	–	0.60	–
Macro precision	0.80	0.56	0.68
Recall C1	0.84	0.57	0.6
Recall C2	0.75	0.31	0.78
Recall C3	–	0.51	–
Recall C4	–	0.77	–
Macro recall	0.79	0.54	0.68
F1 score C1	0.80	0.52	0.6
F1 score C2	0.79	0.38	0.78
F1 score C3	–	0.59	–
F1 score C4	–	0.67	–
Macro F1 score	0.79	0.56	0.68

although it remains comparable to FC. Moreover, the performance metrics for the classification using frequency metrics are shown in Table 7. In terms of accuracy, UMAP outperformed this method with the highest accuracy score of 0.86. TCN matched the classical method accuracy at 0.79, while all FCN models and KAN achieved slightly lower accuracy at 0.66–0.71. This indicates that UMAP and TCN are generally more effective than more complex networks and frequency metrics in accurately detecting VF signals in this dataset.

To demonstrate that the differences in performance between different methods considering UMAP, TCN, FCN n3 and KAN are not due to random chance, we have applied bootstrap resampling and performed pairwise comparison using the Wilcoxon signed-rank test. For each of the three datasets, we generated 1000 bootstrap samples by resampling from the test set and calculating predictions for each method. We then used the Wilcoxon signed-rank test to evaluate pairwise accuracy comparisons between methods, assessing whether the observed differences are statistically significant.

For the surgical VF dataset, UMAP results are statistically significant with a p-value < 0.05 compared to TCN, FC n3 and KAN, while FC n3 demonstrated a statistically significant detection over TCN and KAN. For the dataset treated with different drugs, TCN is statistically significant compared to the rest of the methods, while UMAP is statistically significant compared to FC n3. Finally, for the sustained and non-sustained VF datasets from DAI, UMAP is statistically significant with a p-value < 0.05 compared to TCN, FC n3 and KAN. At the same time, TCN is statistically significant compared to FC n3 and KAN. These statistical distinctions are maintained across datasets, highlighting consistency in method rankings and identifying the best-performing model in each case that varies across datasets.

Moreover, we compared our approach to an established method used to capture long-range dependencies across time series, which is LSTMs. As shown in Table 8, LSTMs achieve comparable performance to TCNs and FCNs in the test set, with high accuracy on the surgical dataset (outperforming TCNs and matching FCNs), while on the two other datasets, they perform similarly to FCNs but fall slightly behind TCNs. Therefore, we can conclude that our proposed methodology aligns well with current approaches for this type of data.

3.2. Results on embedding estimators

UMAP was used primarily for visualization and interpretation of the high-dimensional data. It was applied not only to the methods themselves but also to visualize the activation functions of the last layer of the TCN, the bottleneck layers of the FCNs, and the activations of KANs.

Fig. 3 displays the embedding spaces generated for the surgical VF detection task. The UMAP embeddings separate the two classes in both the training and test sets. The embeddings generated from the activations of the last layer of the TCN demonstrate a separation between classes in the training set, but the classes are not distinctly clustered. Moreover, the spatial distribution of the classes in the test set is not maintained in the training set. The embeddings from the FCN with a bottleneck of three dimensions also show separation between the classes in both sets. Finally, from KAN, the embeddings are more compact and exhibit some degree of overlap. For higher-dimensional FCN bottlenecks of 5, 10, and 15, UMAP was applied to reduce the dimensions to three for visualization. In all three cases, the embeddings show a similar pattern, with a separation between VFON and VFOFF classes and minimal overlap, especially for the FCN with a bottleneck of 10 dimensions, as shown in Fig. 4.

Fig. 5 displays the embedding spaces generated for the VF detection task in dogs, categorized into four classes. In the embeddings, class C1 (Flecainide) and class C2 (Amiodarone) overlap across all methods, making them indistinguishable. However, these classes are separated from Diltiazem and Controls. In the TCN embeddings, no large clusters are formed. However, there is a separation between the classes. Among the FCNs, the best results are observed with a bottleneck dimension of 10, but the differences are minimal compared to other bottleneck dimensions. Regardless of the bottleneck size, the overlap between classes 1 and 2 persists, as shown in Fig. 6. As seen in the metrics results, this overlap negatively impacts accuracy and precision performance. The consistent overlap between Flecainide and Amiodarone in the embeddings suggests similar effects of these drugs on VF, which could be valuable for understanding how these treatments influence the electrical activity of the heart during VF episodes. Moreover, in our analysis, the signals from the dogs have a duration of 360 s. We considered the last 120 s, where class differences are more pronounced. This focus is due to the initial part of the signals (the first 120 s) showing significant overlap with no clear distinctions. This observation suggests an evolution in the frequency characteristics of the signals, which becomes more accentuated towards the end. This evolution may contribute to the observed confusion between classes.

The embedding spaces generated by UMAP demonstrate superior performance in distinguishing between the two classes for the sustained and non-sustained VF datasets from DAI. UMAP effectively creates distinct clusters for both VF classes, allowing for better interpretability and visualization. In contrast, the TCN embeddings fail to produce two separate clusters, indicating difficulty in accurately differentiating the classes, as seen in Fig. 7. In Fig. 8, the results obtained from the higher-dimensional fully connected networks show a similar level of separation, although the clusters appear in different parts of the space.

4. Discussion and conclusion

In this study, we investigated the use of advanced analytical methods, particularly MnL techniques, and deep learning approaches, to classify and interpret the underlying dynamics of VF. Our primary focus is advancing clinical knowledge by exploring the different evolutions in VF based on frequency, with MnL better identifying the features for these distinctions. The application of MnL across different methods is particularly valuable, as it enables the visualization of network embeddings where activation functions can vary. Specifically, in KAN, activation functions are learnable at the edges between neurons,

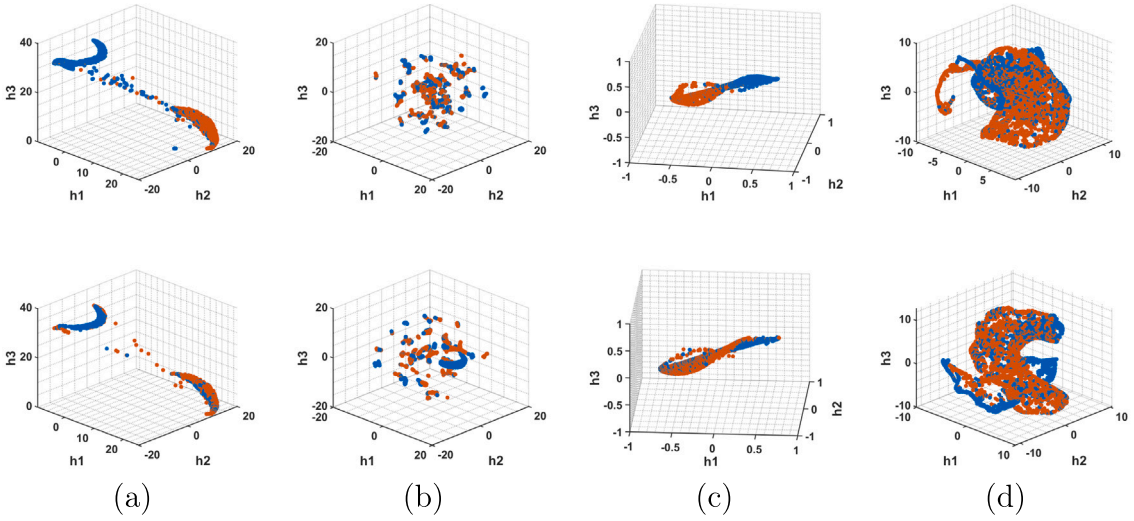

Fig. 3. Embedding spaces of classifiers for surgical VF detection. The top row represents the training set embeddings, while the bottom row represents the test set embeddings. Blue points indicate VFOFF (Class C1), and red points indicate VFON (Class C2): (a) UMAP embeddings; (b) Embeddings from the activations of the last layer of the TCN; (c) Embeddings from the FCN with a bottleneck of three dimensions; (d) Embeddings from the activations of KAN.

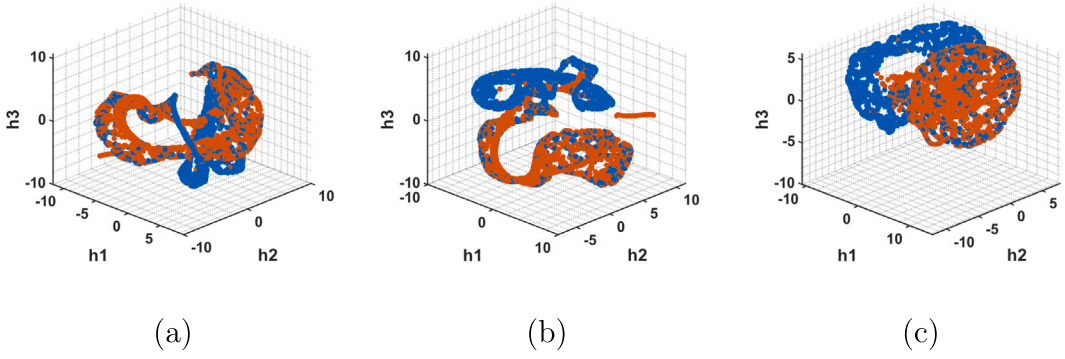

Fig. 4. Embedding spaces of FCNs classifiers with different bottleneck dimensions. Blue points indicate VFOFF (Class C1), and red points indicate VFON (Class C2): (a) Bottleneck dimension of 5; (b) Bottleneck dimension of 10; (c) Bottleneck dimension of 15.

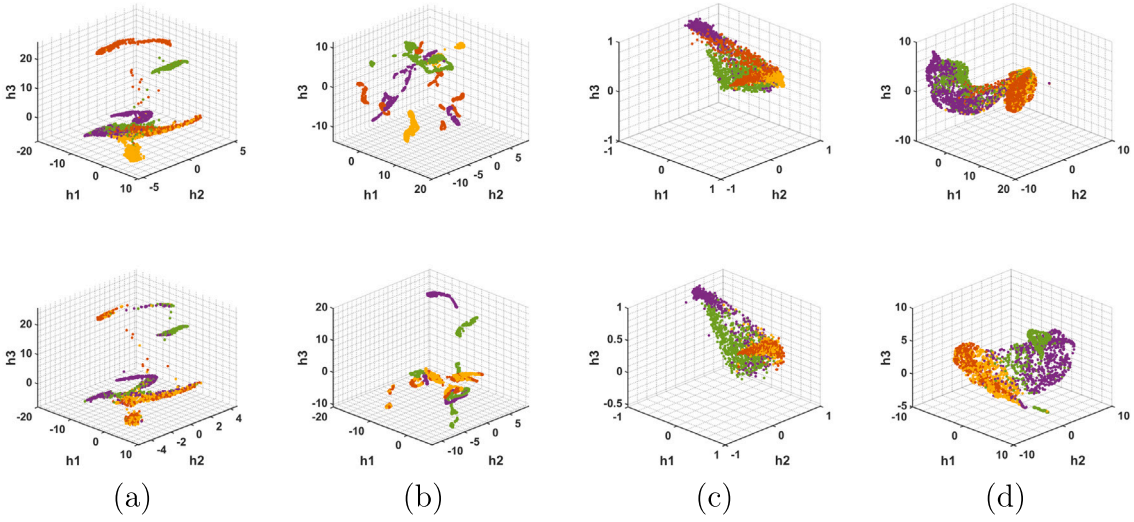

Fig. 5. Embedding spaces of classifiers for VF detection based on different drugs. The top row represents the training set embeddings, while the bottom row represents the test set embeddings. Red points indicate Flecainide (Class C1), yellow points indicate Amiodarone (Class C2), green points indicate Diltiazem (Class C3), and purple points indicate the control group (Class C4): (a) UMAP embeddings; (b) Embeddings from the activations of the last layer of the TCN; (c) Embeddings from the FCN with a bottleneck of three dimensions; (d) Embeddings from the activations of KAN.

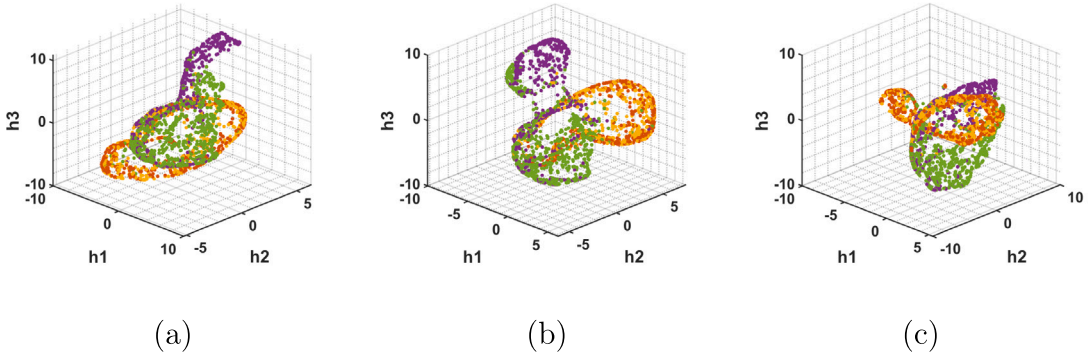

Fig. 6. Embedding spaces of FCN classifiers with different bottleneck dimensions. Red points indicate Flecainide (Class C1), yellow points indicate Amiodarone (Class C2), green points indicate Diltiazem (Class C3), and purple points indicate the control group (Class C4): (a) Bottleneck dimension of 5; (b) Bottleneck dimension of 10; (c) Bottleneck dimension of 15.

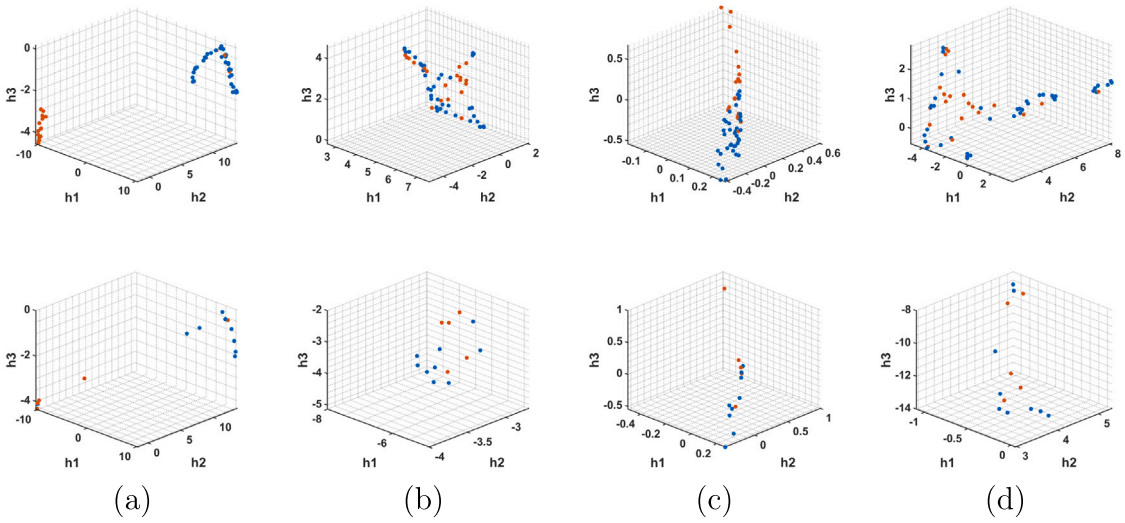

Fig. 7. Embedding spaces of classifiers for sustained and non-sustained VF detection. The top row represents the training set embeddings, while the bottom row represents the test set embeddings. Blue points indicated sustained VF (Class C1) while red points indicate non-sustained VF (Class C2): (a) UMAP embeddings; (b) Embeddings from the activations of the last layer of the TCN; (c) Embeddings from the FCN with a bottleneck of three dimensions; (d) Embeddings from the activations of KAN.

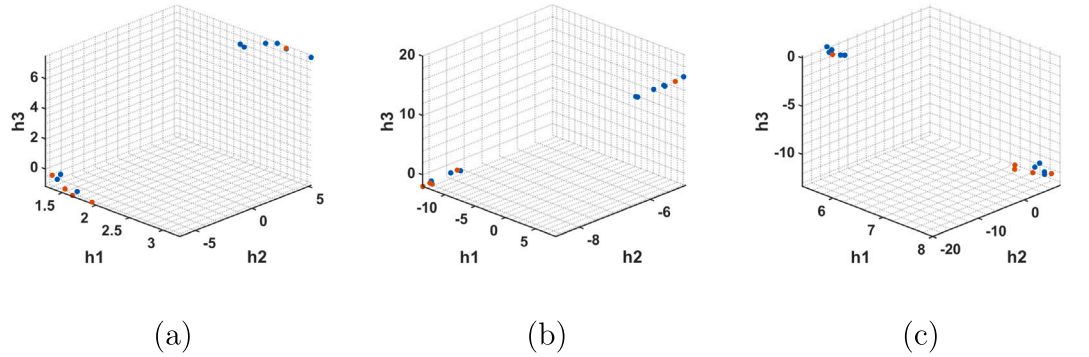

Fig. 8. Embedding spaces of FCN classifiers with different bottleneck dimensions. Blue points indicated sustained VF (Class C1) while red points indicated non-sustained VF (Class C2): (a) Bottleneck dimension of 5; (b) Bottleneck dimension of 10; (c) Bottleneck dimension of 15.

whereas in TCN and FC networks, they operate within the neurons themselves. KAN networks are known for their interpretability due to the derivation of explicit equations. However, in our case, due to the high input size, these equations are not useful for interpretation. Across all methods and datasets, we observed consistency in classification performance within a certain range, as well as an embedding representation where some classes formed separate clusters, while others overlapped.

At this stage, we are not yet addressing practical implementation in real-world hospital settings, instead aiming to provide valuable information that could guide future research and clinical approaches. Moreover, due to their differing nature and context, the datasets used cannot be directly compared in terms of classification performance. This is

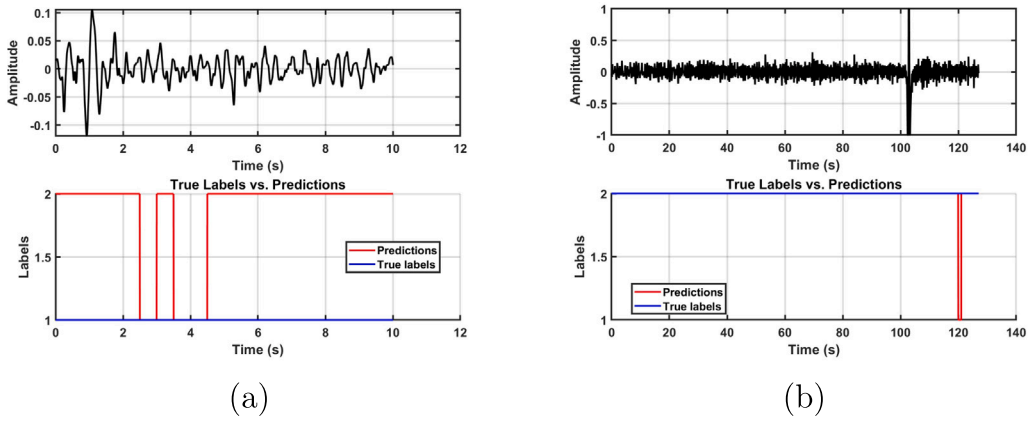

Fig. 9. Impact of signal length: (a) Shorter signal segments lead to higher misclassification rates; (b) Longer signals provide more frequency information, resulting in fewer misclassifications.

because two datasets involve human subjects, while the third consists of recordings from canines undergoing various pharmacological treatments.

Our results demonstrated that the separability of VF types is significantly accentuated in longer signals where the frequency evolution can be observed more clearly. For instance, in clinical settings involving CPB procedures, we analyzed signals with an average length of 138.29 s. These longer signals allowed us to observe distinct frequency evolution patterns, enabling the classification of VF types. However, shorter signals, particularly those from 6 s to 10 s duration for VFON, were often misclassified. This misclassification likely indicates a lack of sufficient frequency evolution, thereby underscoring the importance of signal duration in accurately identifying VF types. In Fig. 9, the impact of signal length on the UMAP methodology is shown. As observed, longer signals exhibit a clearer frequency evolution.

In the dataset involving dogs treated with different drugs, the complete recorded signals were 360 s long, but we focused on the last 120 s, where differences between groups appeared. Interestingly, the differences were not evident during the first 120 s of the recordings. Differences started to appear in the middle part of the signal but were not as pronounced as in the final segment. This observation suggests that the critical frequency evolution necessary for distinguishing VF types occurs later in the signal, where the signals are longer and the frequency evolution and change are more evident.

Finally, the average signal duration for the analysis of sustained and non-sustained VF signals from the ICD was 7.544 s. Our initial approach involved using overlapping windows to examine the frequency evolution of these signals, which was consistent with the methods applied to the previous dataset. However, more apparent separation between VF types was not observed with this approach. Consequently, we chose to visualize the frequency information to detect any differences better. In this way, differences between sustained and non-sustained VF appeared.

The results regarding VF during CPB can be clinically interpreted. Our findings demonstrate a clear separation between VFON and VFOFF conditions, which was evident in both the embeddings and performance metrics. This separation is consistent with previous research using this dataset that employed spectral and nonlinear parameters, such as f_d, regularity index (ri), and nonlinear index sample entropy ($SampEn$), to differentiate between VFON (pre-surgery) and VFOFF (post-surgery) conditions. This study primarily relied on statistical metrics applied to 5-s segments at the beginning and end of the VF signals. The results showed that at the beginning of the VF episodes, only the spectral index ri showed a statistically significant increase. At the end of the VF episodes, f_d increased significantly by approximately 1 Hz on average, and $SampEn$ reflected higher irregularity and complexity after surgery (VFOFF) (Pulido-Hidalgo et al., 2013).

Our findings align with existing literature that characterizes the evolution of VF in the frequency domain for dogs treated with different drugs. As previously mentioned, differences appear in the last part of the signal, with amiodarone and flecainide showing similar frequency evolution as indicated by their overlap in the embeddings. At the same time, there are more pronounced differences with diltiazem. Previous research on this dataset also analyzed the temporal evolution of f_d to study the impact of different drugs on VF dynamics using statistical tests to identify significant differences across time intervals. These studies showed that f_d typically increased during the initial seconds of VF, followed by a progressive decrease as the spectrum became more disorganized. Initial frequencies in control groups were reported at approximately 8.37 ± 1.22 Hz, with significant changes occurring after 90 s. Specifically, diltiazem increased the f_d of VF and diminished the arrhythmia-slowing process, whereas amiodarone and flecainide showed an arrhythmia-slowing effect, reducing the f_d of VF. The statistical results reveal that the f_d values in the diltiazem group were significantly higher than those in the flecainide group throughout the entire arrhythmia (p-value < 0.05). Similarly, f_d values in the diltiazem group were significantly higher than those in the amiodarone group during key intervals, including the initial phase, 15 s, 120 s, and up to 300 s (p-value < 0.05). These results demonstrate that diltiazem not only increases the f_d but also exhibits a distinct electrophysiological effect compared to amiodarone and flecainide (Chorro et al., 1996). Regarding the action of amiodarone and flecainide, Class III agents significantly reduced f_d in episodes of VF induced during ICD testing (Panfilov et al., 2009). Another study analyzing VF from ICD showed that VT/VF episodes with the Class III antiarrhythmic drug amiodarone displayed lower f_d than episodes without the drug (Calvo et al., 2022). In this way, flecainide diminished the f_d during VF in an animal model (Chorro et al., 2000). Therefore, these findings suggest that the electrophysiological actions of these drugs significantly impact the frequency dynamics of VF, with flecainide and amiodarone clustering together in the embeddings due to their similar reduction of the f_d. Analyzing how different drugs (amiodarone, diltiazem, and flecainide) modify the frequency dynamics of VF helps identify which drugs may be most effective in controlling or slowing down fibrillatory activity, improving antiarrhythmic treatment based on their effects on VF dynamics.

Finally, our study investigated the differences in VF termination by examining the complete spectrum of VF signals, revealing notable distinctions between sustained and non-sustained VF episodes. In this way, a previous study analyzed f_d, the power of the dominant frequency and its harmonics, and the organization index (OI) which were used as metrics for comparison. These parameters were analyzed statistically, and the results indicated that sustained VF episodes presented a significantly larger f_d than non-sustained VF episodes (4.6 ± 0.7 Hz

vs. 4.3 ± 0.6 Hz, respectively). However, the powers of the dominant frequency, its harmonics, and the OI were found to be similar in both groups (SánchezMuñoz et al., 2009). Likewise, Calvo et al. showed that the average f_d was lower in self-terminated than shock-terminated episodes of VF recorded by ICD (Calvo et al., 2022). The differences between sustained and non-sustained VF could provide information on the mechanisms of VF and help the development of new algorithms in implantable automatic defibrillators to avoid therapies in case of self-limiting fibrillations.

In conclusion, our study underscores the ability of MnL and deep learning methods using frequency evolution to distinguish between different subtypes of VF that could enhance the understanding of VF pathophysiology in diverse clinical contexts. Our findings demonstrate that longer signals provide a clearer differentiation between VF types as the frequency evolution becomes more evident over extended periods. This highlights the importance of signal duration in accurately identifying VF types. Moreover, the results obtained with the proposed methods are clinically interpretable.

CRediT authorship contribution statement

Dafne Lozano-Paredes: Writing – review & editing, Writing – original draft, Visualization, Software, Methodology, Investigation, Formal analysis. **Juan José Sánchez-Muñoz:** Writing – review & editing, Validation, Supervision, Investigation, Data curation, Conceptualization. **Luis Bote-Curiel:** Writing – review & editing, Validation, Supervision, Software, Methodology. **Francisco M. Melgarejo-Meseguer:** Writing – review & editing, Validation, Supervision, Software, Methodology, Data curation. **Antonio Gil-Izquierdo:** Data curation. **F. Javier Gimeno-Blanes:** Writing – review & editing, Data curation. **José Luis Rojo-Álvarez:** Writing – review & editing, Validation, Supervision, Resources, Project administration, Investigation, Funding acquisition, Data curation.

Declaration of competing interest

The authors declare that they have no known competing financial interests or personal relationships that could have appeared to influence the work reported in this paper.

Acknowledgments

This work was partially supported by Research Grants meHeart, PCardioTrials, LATENTIA and HERMES (PID2019-104356RB-C42, PID2022-140553OA-C42, PID2022-140786NB-C31, and PID2023-152331OA-I00) funded by AEI/10.13039/501100011033. Additionally, it was supported by research Grant HERMES 2024/00004/006, Ref: F1083, from Rey Juan Carlos University. Thanks to Profs. Jesús Requena-Carrión, Óscar Barquero-Pérez, Paúl Bernal-Oñate, and Vinicio Carrera, for their kind support with data recovery and precedent analysis.

Data availability

The data that has been used is confidential.

References

Afonso, V., Tompkins, W., 1995. Detecting ventricular fibrillation. IEEE Eng. Med. Biol. Mag. 14 (2), 152–159. http://dx.doi.org/10.1109/51.376752.

Amann, A., Rheinberger, K., Achleitner, U., 2001. Algorithms to analyze ventricular fibrillation signals. Curr. Opin. Crit. Care 7 (3), 152–156. http://dx.doi.org/10.1097/00075198-200106000-00003.

Arafat, M.A., Chowdhury, A.W., Hasan, M.K., 2011. A simple time domain algorithm for the detection of ventricular fibrillation in electrocardiogram. Signal Image Video Process. 5 (1), 1–10. http://dx.doi.org/10.1007/s11760-009-0136-1.

Bai, S., Kolter, J.Z., Koltun, V., 2018. An empirical evaluation of generic convolutional and recurrent networks for sequence modeling. arXiv preprint arXiv:1803.01271.

Barquero-Pérez, Ó., Rojo-Álvarez, J.L., Caamaño, A.J., Goya-Esteban, R., Everss, E., Alonso-Atienza, F., Sánchez-Muñoz, J.J., García-Alberola, A., 2010. Fundamental frequency and regularity of cardiac electrograms with Fourier organization analysis. IEEE Trans. Biomed. Eng. 57 (9), 2168–2177. http://dx.doi.org/10.1109/TBME.2010.2049574.

Bernal Oñate, C.P., Melgarejo Meseguer, F.-M., Carrera, E.V., Sánchez Muñoz, J.J., García Alberola, A., Rojo Álvarez, J.L., 2023. Different ventricular fibrillation types in low-dimensional latent spaces. Sensors 23 (5), http://dx.doi.org/10.3390/s23052527.

Calvo, D., Salinas, L., Martínez-Camblor, P., García-Iglesias, D., Alzueta, J., Rodríguez, A., Romero, R., Viñolas, X., Fernández-Lozano, I., Anguera, I., Villacastín, J., Bodegas, A., Fontenla, A., Jalife, J., Berenfeld, O., 2022. Distinct spectral dynamics of implanted cardiac defibrillator signals in spontaneous termination of polymorphic ventricular tachycardia and fibrillation in patients with electrical and structural diseases. EP Eur. 24 (11), 1788–1799. http://dx.doi.org/10.1093/europace/euac107.

Chorro, F.J., Cánoves, J., Guerrero, J., Mainar, L., Sanchis, J., Such, L., López-Merino, V., 2000. Alteration of ventricular fibrillation by Flecainide, Verapamil, and Sotalol. Circ. 101 (13), 1606–1615. http://dx.doi.org/10.1161/01.CIR.101.13.1606.

Chorro, F.J., Sánchez-Muñoz, J.J., Sanchis, J., Cortina, J., Bataller, M., Guerrero, J., Espí, J., Ruipérez, J.A., López-Merino, V., 1996. Modifications in the evolution of the dominant frequency in ventricular fibrillation induced by amiodarone, diltiazem, and flecainide: An experimental study. J. Electrocardiol. 29 (4), 319–326. http://dx.doi.org/10.1016/S0022-0736(96)80096-3.

de Luna, A.B., Coumel, P., Leclercq, J.F., 1989. Ambulatory sudden cardiac death: Mechanisms of production of fatal arrhythmia on the basis of data from 157 cases. Am. Heart J. 117 (1), 151–159. http://dx.doi.org/10.1016/0002-8703(89)90670-4.

Dharmaprani, D., Jenkins, E.V., Quah, J.X., Lahiri, A., Tiver, K., Mitchell, L., Bradley, C.P., Hayward, M., Paterson, D.J., Taggart, P., Clayton, R.H., Nash, M.P., Ganesan, A.N., 2022. A governing equation for rotor and wavelet number in human clinical ventricular fibrillation: Implications for sudden cardiac death. Hear. Rhythm. 19 (2), 295–305. http://dx.doi.org/10.1016/j.hrthm.2021.10.008.

Din, S., Qaraqe, M., Mourad, O., Qaraqe, K., Serpedin, E., 2024. ECG-based cardiac arrhythmias detection through ensemble learning and fusion of deep spatial–temporal and long-range dependency features. Artif. Intell. Med. 150, 102818. http://dx.doi.org/10.1016/j.artmed.2024.102818.

Garfinkel, A., Kim, Y.-H., Voroshilovsky, O., Qu, Z., Kil, J.R., Lee, M.-H., Karagueuzian, H.S., Weiss, J.N., Chen, P.-S., 2000. Preventing ventricular fibrillation by flattening cardiac restitution. Proc. Natl. Acad. Sci. 97 (11), 6061–6066. http://dx.doi.org/10.1073/pnas.090492697.

Gaztañaga, L., Marchlinski, F.E., Betensky, B.P., 2012. Mechanisms of cardiac arrhythmias. Rev. Esp. Cardiol. (Engl. Ed.) 65 (2), 174–185. http://dx.doi.org/10.1016/j.rec.2011.09.020.

Goodfellow, I., Bengio, Y., Courville, A., 2016. Deep Learning. MIT Press, URL http://www.deeplearningbook.org.

Haïssaguerre, M., 2010. In search of the sources of cardiac fibrillation. EMBO Mol. Med. 2 (4), 117–119. http://dx.doi.org/10.1002/emmm.201000066.

Haïssaguerre, M., Vigmond, E., Stuyvers, B., Hocini, M., Bernus, O., 2016. Ventricular arrhythmias and the His–Purkinje system. Nat. Rev. Cardiol. 13 (3), 155–166. http://dx.doi.org/10.1038/nrcardio.2015.193.

Hassan, S.U., Abdulkadir, S.J., Mohd Zahid, M.S., Fayyaz, A.M., Al-Selwi, S.M., Sumiea, E.H., 2024. An optimized CNN-LSTM model for detecting cardiac arrhythmias. In: 2024 IEEE 8th International Conference on Signal and Image Processing Applications. ICSIPA, pp. 1–6. http://dx.doi.org/10.1109/ICSIPA62061.2024.10686688.

Jalife, J., 2000. Ventricular fibrillation: Mechanisms of initiation and maintenance. Annu. Rev. Physiol. 62, 25–50. http://dx.doi.org/10.1146/annurev.physiol.62.1.25.

Jekova, I., Krasteva, V., 2004. Real time detection of ventricular fibrillation and tachycardia. Physiol. Meas. 25 (5), 1167. http://dx.doi.org/10.1088/0967-3334/25/5/007.

John, R.M., Tedrow, U.B., Koplan, B.A., Albert, C.M., Epstein, L.M., Sweeney, M.O., Miller, A.L., Michaud, G.F., Stevenson, W.G., 2012. Ventricular arrhythmias and sudden cardiac death. Lancet 380 (9852), 1520–1529. http://dx.doi.org/10.1016/S0140-6736(12)61413-5.

Kingma, J., Simard, C., Drolet, B., 2023. Overview of cardiac arrhythmias and treatment strategies. Pharm. (Basel) 16 (6), 844. http://dx.doi.org/10.3390/ph16060844.

Latcu, G.D., Meste, O., Duparc, A., Mondoly, P., Rollin, A., Delay, M., Maury, P., 2011. Temporal and spectral analysis of ventricular fibrillation in humans. J. Interv. Card. Electrophysiol. 30 (3), 199–209. http://dx.doi.org/10.1007/s10840-010-9541-1.

Li, Q., Rajagopalan, C., Clifford, G.D., 2014. Ventricular fibrillation and tachycardia classification using a machine learning approach. IEEE Trans. Biomed. Eng. 61 (6), 1607–1613. http://dx.doi.org/10.1109/TBME.2013.2275000.

Link, M.S., Berkow, L.C., Kudenchuk, P.J., Halperin, H.R., Hess, E.P., Moitra, V.K., Neumar, R.W., O'Neil, B.J., Paxton, J.H., Silvers, S.M., White, R.D., Yannopoulos, D., Donnino, M.W., 2015. Part 7: Adult advanced cardiovascular life support. Circ. 132 (18 Suppl 2), S444–S464. http://dx.doi.org/10.1161/CIR.0000000000000261.

Liu, Z., Wang, Y., Vaidya, S., Ruehle, F., Halverson, J., Soljačić, M., Hou, T.Y., Tegmark, M., 2024. Kan: Kolmogorov-Arnold networks. arXiv preprint arXiv:2404.19756.

McInnes, L., Healy, J., Saul, N., Großberger, L., 2018. UMAP: Uniform manifold approximation and projection. J. Open Source Softw. 3 (29), 861. http://dx.doi.org/10.21105/joss.00861.

Mjahad, A., Rosado-Muñoz, A., Guerrero-Martínez, J.F., Bataller-Mompeán, M., Francés-Villora, J.V., Dutta, M.K., 2018. Detection of ventricular fibrillation using the image from time-frequency representation and combined classifiers without feature extraction. Appl. Sci. 8 (11), 2057. http://dx.doi.org/10.3390/app8112057.

Moe, G.K., Rheinboldt, W.C., Abildskov, J., 1964. A computer model of atrial fibrillation. Am. Heart J. 67 (2), 200–220. http://dx.doi.org/10.1016/0002-8703(64)90371-0.

Nash, M.P., Mourad, A., Clayton, R.H., Sutton, P.M., Bradley, C.P., Hayward, M., Paterson, D.J., Taggart, P., 2006. Evidence for multiple mechanisms in human ventricular fibrillation. Circ. 114 (6), 536–542. http://dx.doi.org/10.1161/CIRCULATIONAHA.105.602870.

Pandit, S.V., Jalife, J., 2013. Rotors and the dynamics of cardiac fibrillation. Circ. Res. 112 (5), 849–862. http://dx.doi.org/10.1161/CIRCRESAHA.111.300158.

Panfilov, I., Lever, N.A., Smaill, B.H., Larsen, P.D., 2009. Ventricular fibrillation frequency from implanted cardioverter defibrillator devices. EP Eur. 11 (8), 1052–1056. http://dx.doi.org/10.1093/europace/eup159.

Pham, T.-H., Sree, V., Mapes, J., Dua, S., Lih, O.S., Koh, J.E.W., Ciaccio, E.J., Acharya, U.R., 2021. A novel machine learning framework for automated detection of arrhythmias in ECG segments. J. Ambient. Intell. Humaniz. Comput. 12 (11), 10145–10162. http://dx.doi.org/10.1007/s12652-020-02779-1.

Pulido-Hidalgo, F.J., Barquero-Pérez, Ó., Soguero-Ruiz, C., Sánchez-Muñoz, J.J., Rojo-Álvarez, J.L., García-Alberola, A., 2013. Spectral and nonlinear analysis of surgical ventricular fibrillation. In: 2013 Computing in Cardiology Conference. pp. 1123–1126.

Sabut, S., Pandey, O., Mishra, B.S.P., Mohanty, M., 2021. Detection of ventricular arrhythmia using hybrid time–frequency-based features and deep neural network. Phys. Eng. Sci. Med. 44 (1), 135–145. http://dx.doi.org/10.1007/s13246-020-00964-2.

Sahoo, S., Dash, M., Behera, S., Sabut, S., 2020. Machine learning approach to detect cardiac arrhythmias in ECG signals: A survey. IRBM 41 (4), 185–194. http://dx.doi.org/10.1016/j.irbm.2019.12.001.

SánchezMuñoz, J.J., Luis Rojo Álvarez, J., García Alberola, A., Everss, E., Alonso-Atienza, F., Ortiz, M., Martínez Sánchez, J., Ramos-López, J., Valdés Chávarri, M., 2008. Spectral analysis of intracardiac electrograms during induced and spontaneous ventricular fibrillation in humans. EP Eur. 11 (3), 328–331. http://dx.doi.org/10.1093/europace/eun366.

SánchezMuñoz, J.J., Luis Rojo Álvarez, J., García Alberola, A., Requena Carrión, J., Everss, E., Ortiz, M., Martínez Sánchez, J., Valdés Chávarri, M., 2009. Spectral analysis of sustained and non-sustained ventricular fibrillation in patients with an implantable cardioverter-defibrillator. Rev. Esp. Cardiol. (Engl. Ed.) 62 (6), 690–693. http://dx.doi.org/10.1016/s1885-5857(09)72234-0.

Stewart, A., Allen, J., Adgey, A., 1992. Frequency analysis of ventricular fibrillation and resuscitation success. QJM: Int. J. Med. 85 (1), 761–769.

Taye, G.T., Shim, E.B., Hwang, H.-J., Lim, K.M., 2019. Machine learning approach to predict ventricular fibrillation based on QRS complex shape. Front. Physiol. 10, 1193. http://dx.doi.org/10.1371/journal.pone.0207215.

Tseng, L.-M., Tseng, V.S., 2020. Predicting ventricular fibrillation through deep learning. IEEE Access 8, 221886–221896. http://dx.doi.org/10.1109/ACCESS.2020.3042782.

Vaneghi, F.M., Oladazimi, M., Shiman, F., Kordi, A., Safari, M., Ibrahim, F., 2012. A comparative approach to ECG feature extraction methods. In: 2012 Third International Conference on Intelligent Systems Modelling and Simulation. pp. 252–256. http://dx.doi.org/10.1109/ISMS.2012.35.

Walton, R.D., Martinez, M.E., Bishop, M.J., Hocini, M., Haïssaguerre, M., Plank, G., Bernus, O., Vigmond, E.J., 2014. Influence of the Purkinje-muscle junction on transmural repolarization heterogeneity. Cardiovasc. Res. 103 (4), 629–640. http://dx.doi.org/10.1093/cvr/cvu165.